Supporting Information

Hybrid magneto-dynamical modes in a single magnetostrictive nanomagnet on a piezoelectric substrate arising from magneto-elastic modulation of precessional dynamics

Sucheta Mondal[1], Md Ahsanul Abeed[2], Koustuv Dutta[1], Anulekha De[1], Sourav Sahoo[1], Anjan Barman[1, *] and Supriyo Bandyopadhyay[2, *]

[1]Department of Condensed Matter Physics and Material Sciences, S. N. Bose National Centre for Basic Sciences, Block JD, Sector III, Salt Lake, Kolkata 700 106, India

[2]Department of Electrical and Computer Engineering, Virginia Commonwealth University, Richmond, VA 23284, USA

Corresponding author emails: Anjan Barman (abarman@bose.res.in); Supriyo Bandyopadhyay (sbandy@vcu.edu)

Experimental details

Time-resolved magneto-optical Kerr effect measurements: We have used a two-color pump-probe technique, where the fundamental laser beam generated from a Tsunami (Spectra Physics, λ = 800 nm, pulse width ≈ 80 fs) femtosecond laser is exploited to probe the magnetization dynamics of the sample. In all experiments, the probe fluence is kept fixed at 2 mJ/cm^2 and the pump fluence is varied between 7 and 15 mJ/cm^2. A bias magnetic field is applied at a small angle (ϕ) of about 10^o-15^o with respect to the sample plane (as shown in Fig. 1(c)) in the direction of the ellipses' minor axes to induce precession of the nanomagnet's magnetization around this field upon excitation by the pump beam.

To measure the time-resolved oscillations in the intensity and polarization of the light reflected from the nanomagnet, we use a 1 ns time window with 1 ps temporal resolution, which captures the full time-domain spin dynamics carrying several spin-wave frequencies. The probe beam collects information about dynamic Kerr signal and reflectivity from the sample and sends it to an optical bridge detector (OBD). A polarized beam splitter (PBS) at the entrance of the OBD splits the beam into two orthogonal polarization components. These two parts, with two different intensities (IA and IB**),** are then detected by two photodiodes. The outputs of these two photodiodes are subsequently pre-amplified and used as inputs for two operational amplifiers to measure the total signal A+B (i.e., IA+ IB) and the difference signal A-B (i.e. IA- IB). The outputs of these two Op-Amps are measured by two lock-in-amplifiers in a phase sensitive manner with the chopper frequency as the reference. Initially, in the absence of the pump beam, the optical axis of this PBS is set at 45^o to the plane of polarization of the probe beam making IA = IB, i.e., A-B = 0 and the detector is said to be in a "balanced" condition. In the next step, when the pump beam excites the nanomagnet, the plane of polarization of the probe beam is rotated due to the magneto-optical Kerr effect. Consequently, the optical axis of the PBS is no longer at 45^o to the plane of polarization of the probe beam. As a result, IA ≠ IB and A-B ≠ 0. The linear magneto-optical Kerr rotation is proportional to the sample magnetization, hence to A-B. This can also provide information about the time varying polarization of the substrate. Thus, by measuring A-B as a function of time, magnetization dynamics over different time-scales are observed. The time-varying reflectivity (A+B) can provide information about charge and phonon dynamics.

Micromagnetic Simulation: We have performed micromagnetic simulations using the MuMax3 software. For visualization of the simulated results, we have used MuView software. In the simulation, we have considered an elliptical single nanomagnet with major and minor axes of dimensions 190 nm and 186 nm, and thickness 16 nm. The sample is discretized into cells of dimension 2 × 2 × 16 nm^3. The cell size in the lateral plane is kept below the exchange length of cobalt to reproduce the observed magnetization dynamics. The magnetic parameters used for the simulation are: saturation magnetization M_s= 1100 emu/cm^3, gyromagnetic ratio γ = 17.6 MHz/Oe and exchange stiffness constant A_{ex}= 3.0 × 10^{-5} erg/cm.

In the simulation, the external bias field H is first applied along the minor axis of the nanomagnet to prepare the static micromagnetic distribution by letting the simulation run for 1 ns (enough to obtain steady state). After 1 ns, the magnetization aligns along H almost everywhere within the nanomagnet. Then the SAW-induced periodic strain anisotropy is introduced by making the strain anisotropy energy density $K_1(t) = K_0\left[\sin(2\pi f_1 t) + \sin(2\pi f_2 t)\right]$ where K_0 = 22500 J/m^3 and f_1, f_2 are the frequencies of the two dominant SAW modes (2 GHz and 8 GHz) as shown in Fig. 2 of the text. The parameter K_0 is used as a fitting parameter to obtain the best possible match between simulation and experiment, and the value of K_0 = 22500 J/m^3 provided the best match. In the presence of the applied bias field and the strain-generated effective field, a square pulsed magnetic field of 10 ps rise time, 100 ps width, and peak amplitude of 30

Oe is applied perpendicular to the sample plane to initiate the precession about the bias magnetic field. The resulting simulated magnetization dynamics data are acquired for 1 ns time window.

The MuMax3 simulations are run with a time step of 1 ps and hence provide information about the magnetization of the sample as a function of space (*x, y, z*) every ps. The micromagnetic distributions within the sample at different instants of time (Fig. S4) correspond to the superposition of a number of spin wave modes with varying powers and phases. The profiles in Fig. S4 do not immediately provide information about the individual resonant modes since the MuMax3 simulations yield only the spatial distribution of magnetization as a function of time: *M (t, x, y, z).* After fixing the *z*-coordinate at a particular value $\left(z = z_m\right)$, a discrete Fourier transform (FFT) of $M\left(x, y, z, t\right)\big|_{z=z_m}$ with respect to time is performed to yield $\tilde{M}^{z_m}(f, x, y) = FFT\left[M(x, y, z, t)\big|_{z=z_m}\right]$. The frequency resolution in the FFT depends upon the total simulation time. Spatial resolution depends upon the cell size of the system adopted during the MuMax3 simulations. The fixed value of the z-coordinate $\left(z_m\right)$ is chosen to be at the surface of the nanomagnet. Our in-house software *Dotmag* then plots the $\left(x, y\right)$ spatial distribution of the power and phase of the spin waves at chosen frequencies on the surface of the nanomagnet $\left(z = z_m\right)$ according to the following relations:

$$P^{z_m, f_n}(x, y) = 20\log_{10}\tilde{M}^{z_m}\left(f_n, x, y\right);$$

$$\phi^{z_m, f_n}(x, y) = \tan^{-1}\left(\frac{\mathrm{Im}\left(\tilde{M}^{z_m}\left(f_n, x, y\right)\right)}{\mathrm{Re}\left(\tilde{M}^{z_m}\left(f_n, x, y\right)\right)}\right) \quad ,$$

where f_n is the frequency of a resonant mode.

Investigation of surface acoustic wave (SAW) generated in the PMN-PT substrate

The pump beam generates a SAW in the PMN-PT substrate, which gives rise to the variation in time of the polarization of light reflected from the bare PMN-PT substrate. The outputs of two photodiodes (A and B) inside an optical bridge detector provide the reflectivity signal (A+B) and the Kerr oscillation signal (A-B). The reflectivity variation in time (as a function of the delay between the pump and the probe) was shown in the main text. The time variation of the Kerr signal (polarization of reflected light) is shown in Fig. S1(a). After performing FFT of the background-subtracted time-resolved Kerr signal from the substrate, we can obtain the SAW frequencies as shown in Fig. S1(b). The two main frequencies are again 2 and 8 GHz, as in Fig. 2. Thus, the SAW frequencies obtained from the reflectivity signal and Kerr signal agree.

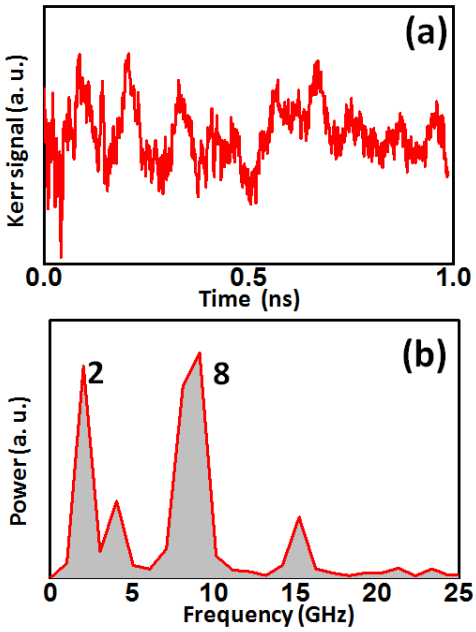

Figure S1: (a) Back ground subtracted time resolved data and (b) Fourier transform (or frequency spectra) of the oscillations in the polarization of light reflected from the bare PMN-PT substrate. The frequencies of the two most intense peaks are indicated in GHz and are the same as in Fig. 2.

Comparison between the amplitudes of the Kerr signal and the reflectivity signal obtained from the periodically strained Co nanomagnet at various bias fields

Figure S2 shows the comparison between the amplitudes of the Kerr oscillation and reflectivity oscillation. The former is two orders of magnitude larger.

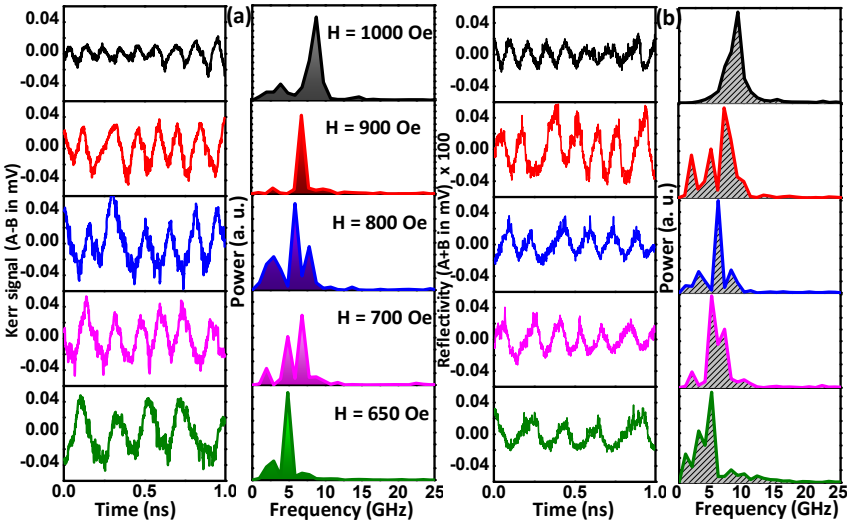

Figure S2: Comparison between the amplitudes of the time-resolved (a) Kerr oscillations (A-B) and (b) reflectivity oscillations (A+B) of a periodically strained single Co nanomagnet on a PMN-PT substrate at different bias magnetic fields. The amplitude of the Kerr oscillations is much larger than that of the reflectivity oscillations. The vertical axis of the A+B (reflectivity) signal has been multiplied by a factor of 100 to make the oscillations visible on this scale. The fluences of pump and probe are 15 mJ/cm^{2}and 2 mJ/cm^2, respectively. The comparison between their Fourier spectra is also shown here.

Time varying SAW-induced strain anisotropy used in the MuMax3 simulation

The SAW-induced periodic strain anisotropy in the nanomagnet is included in the MuMax3 simulation by making the strain anisotropy energy density $K_1(t) = K_0\left[\sin(2\pi f_1 t) + \sin(2\pi f_2 t)\right]$, where f_1, f_2 are the frequencies of the two dominant SAW modes (2 GHz and 8 GHz) observed on the substrate for the pump fluence of 15 mJ/cm^2 used in the experiment. Fig. S3 depicts the time variation of the strain anisotropy energy density. The amplitude of the strain oscillation (K_0) is a fitting parameter in the MuMax3 simulation. The best match between simulation and experiment is obtained for K_0 = 22,500 J/m^3. This single fitting parameter reproduced our experimental results in the low field regime very well, but not in the high field regime. A single parameter is obviously not adequate to match experiment with simulation over a wide bias field range.

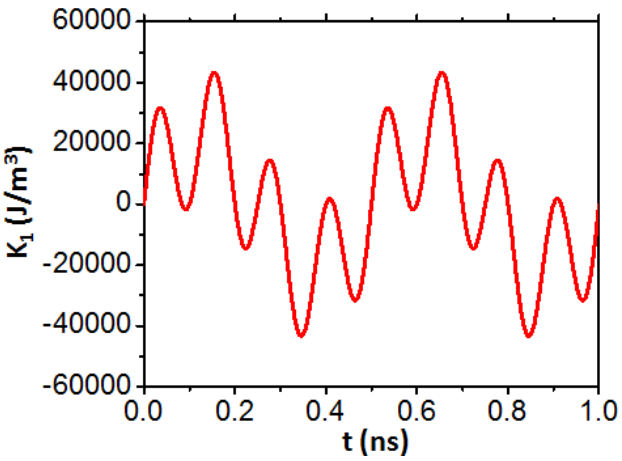

Figure S3: Time varying strain anisotropy energy density (K_1), which is a combination of two sinusoidal oscillations with frequencies 2 and 8 GHz, is shown here.

Simulated micromagnetic distribution profile in the periodically strained nanomagnet at various times

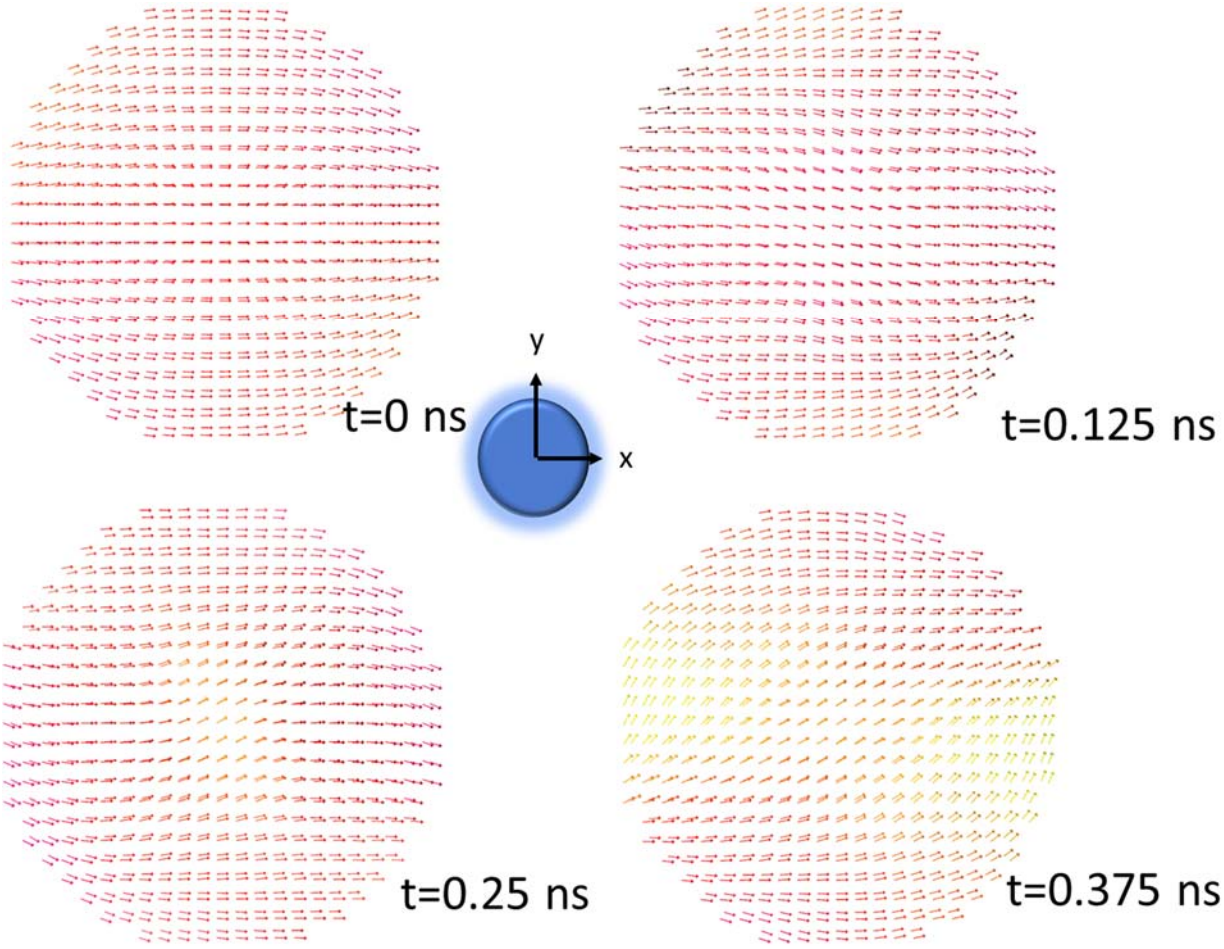

Figure S4(a): Time-lapsed images of the micromagnetic distributions within the Co nanomagnet during the first 0.375 ns obtained from MuMax3 simulations. Time is counted from the instant the time varying strain anisotropy is turned on. The time varying strain anisotropy energy density is again given by $K_1 = 22,500\left[\sin\left(2\pi f_1 t\right)+\sin\left(2\pi f_2 t\right)\right]$; $f_1 = 2$ GHz and $f_2 = 8$ GHz . A bias magnetic field of 760 Oe is directed along the minor axis of the ellipse, pointing to the right. The magnetization is initially assumed to be oriented along the bias field and an out-of-plane square wave tickle field of 30 Oe is turned on at time t = 0 for 100 ps to set the magneto-dynamics in motion.

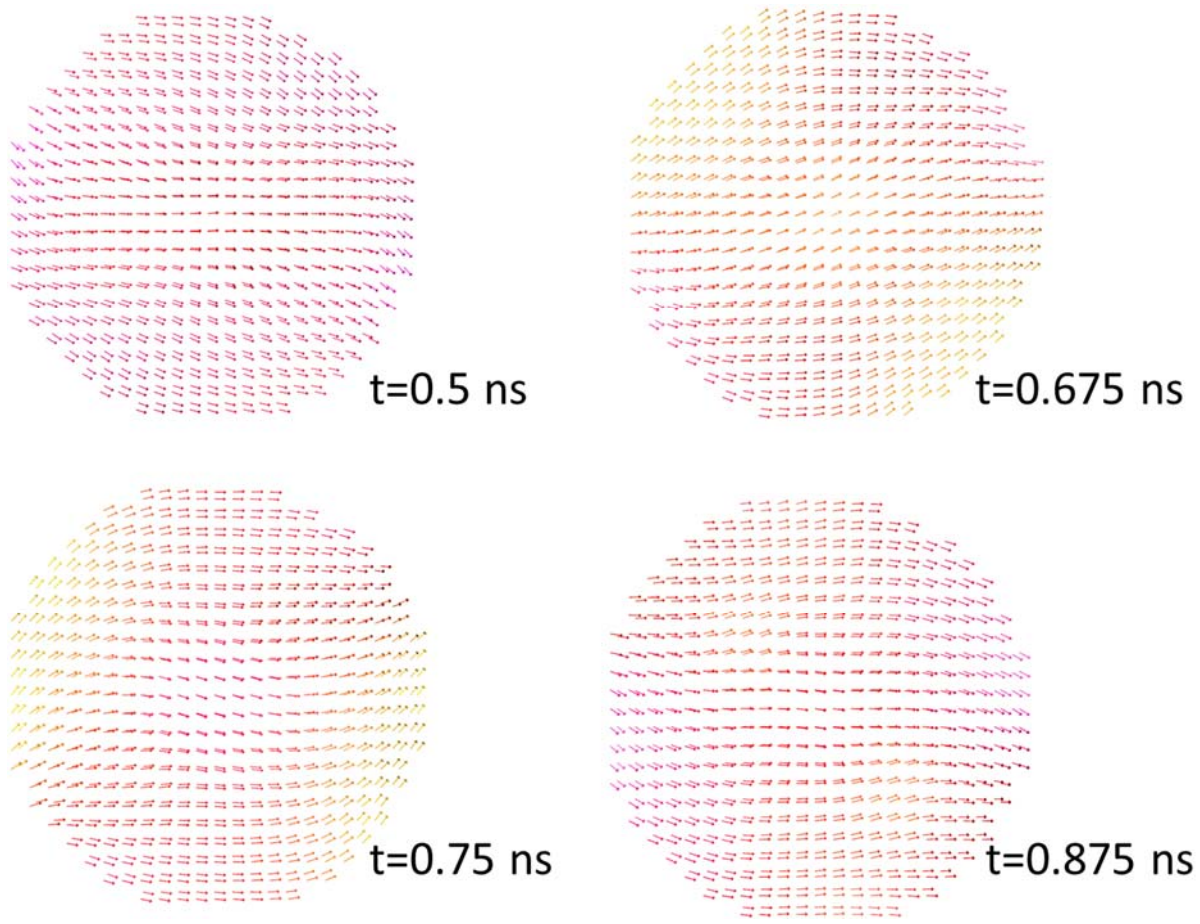

Figure S4(b): Time-lapsed images of the micromagnetic distributions within the Co nanomagnet obtained from MuMax3 simulations. The time varying strain anisotropy energy density is again given by $K_1 = 22,500\left[\sin\left(2\pi f_1 t\right)+\sin\left(2\pi f_2 t\right)\right]$; $f_1 = 2$ GHz and $f_2 = 8$ GHz . A bias magnetic field of 760 Oe is directed along the minor axis of the ellipse, pointing to the right. The magnetization is initially assumed to be oriented along the bias field and an out-of-plane square wave tickle field of 30 Oe is turned on at time t = 0 for 100 ps to set the magneto-dynamics in motion.

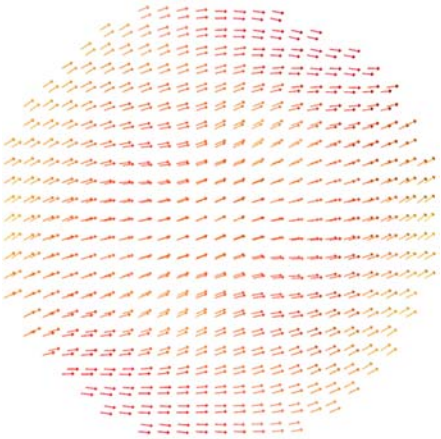

Figure S4(c): Micromagnetic distributions within the Co nanomagnet at 1 ns obtained from MuMax3 simulations. The time varying strain anisotropy energy density is again given by $K_1 = 22{,}500\left[\sin\left(2\pi f_1 t\right)+\sin\left(2\pi f_2 t\right)\right]$; $f_1 = 2$ GHz and $f_2 = 8$ GHz . A bias magnetic field of 760 Oe is directed along the minor axis of the ellipse, pointing to the right. The magnetization is initially assumed to be oriented along the bias field and an out-of-plane tickle field of 30 Oe is turned on at time t = 0 for 100 ps to set the magneto-dynamics in motion.

Simulated spin wave spectra and corresponding mode profile for the *unstrained* Co nanomagnet

Using MuMax3, we obtained the magnetization dynamics of a single *unstrained* Co nanomagnet (no SAWs) at different bias field values for the purpose of comparison with the periodically strained cases. The same simulation parameters are used as in the periodically strained case, except here $K_0 = 0$. In this case, the magneto-dynamics is governed solely by the laser-induced precession of magnetization around the bias magnetic field.

By fast Fourier transforming the spatially averaged out-of-plane magnetization $\bar{M}_z(t)$, we find that the resulting spectrum has two dominant peaks at any bias magnetic field. These two peaks, for a bias field of 1000 Oe, are shown in Fig. S5(a). The Dotmag software provides the power and phase distributions of the spin waves at these two peak frequencies. They are found to be two standing modes - the center mode (mode 2) and the edge mode (mode 1) for every bias field considered (see Fig. S5(c)). The power distributions of these modes (at the center and vertical edges of the nanomagnet) do not change much with bias field. The bias field dependence of the precessional frequency (Fig. S5(b)) reveals that these two modes have excellent stability. We have fitted the dependence using the Kittel formula,

$$f = \frac{\gamma}{2\pi}\sqrt{(H)(H+4\pi M_{eff})}$$

where H is the bias magnetic field. The extracted effective magnetization M_{eff} values from the Kittel fit of the field variation of the center- and edge-modes are 1065 emu/cm^3 and 325 emu/cm^3, respectively. The deviation of M_{eff} values from the intrinsic saturation magnetization of 1100 emu/cm^3 (for Co) can be

explained by the demagnetizing effect from the unsaturated magnetizations at the nanomagnet edges perpendicular to the bias field direction.

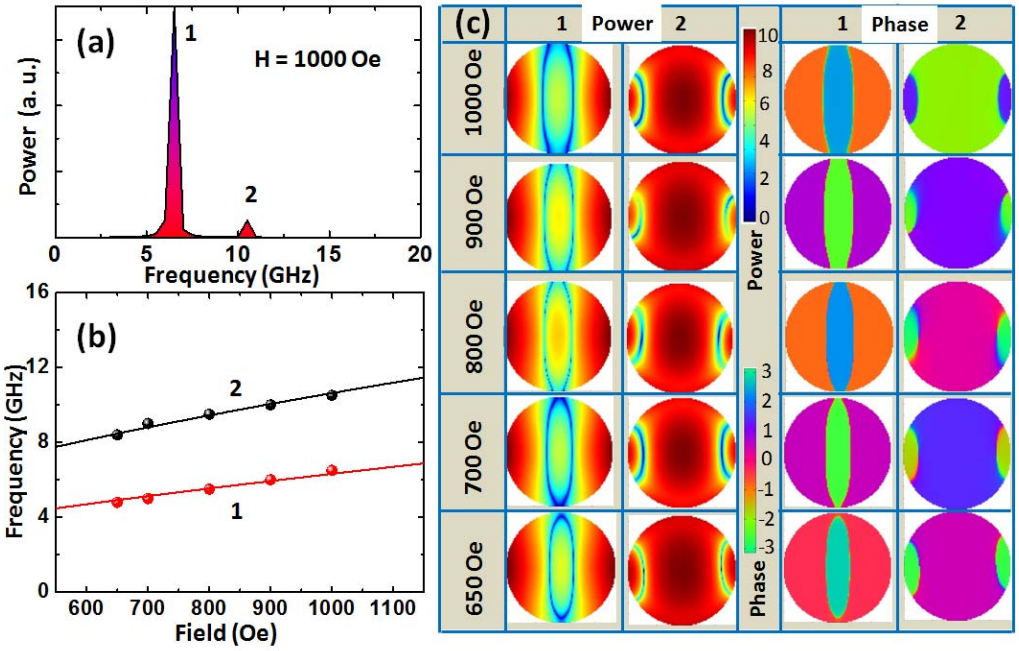

Figure S5: (a) Calculated frequency spectrum of the time variation of the spatially-averaged out-of-plane magnetization component $\bar{M}_z(t)$ in an *unstrained* elliptical Co nanomagnet of major axis 190 nm, minor axis 186 nm and thickness 16 nm, in the presence of a bias magnetic field of 1000 Oe directed along the ellipse's minor axis. The quantity $\bar{M}_z(t)$ is calculated from MuMax3. (b) Bias field dependence of the two peak frequencies observed in the calculated frequency spectrum. Solid lines indicate the Kittel fit. (c) Calculated spin-wave mode profile in the nanomagnet for the two peak frequencies in the spectrum at different bias fields. These profiles are calculated with the Dotmag code. Since the power is concentrated at the center in one mode and vertical edges at the other, they are a 'center mode' and an 'edge mode' and this nature is independent of the bias field in this range. The units of power and phase in this plot are dB and radians, respectively.

A discussion of the two mechanisms that generate SAW in the PMN-PT substrate

There are two mechanisms that generate periodic strain in the PMN-PT substrate and result in a surface acoustic wave – the first is associated with the alternating electric field in the laser generating periodic (compressive and tensile) strain in the PMN-PT substrate from d_{33} and/or d_{31} coupling. The second arises from the (periodic) differential thermal expansions of Co and PMN-PT. Note that the former mechanism requires a piezoelectric substrate, while the latter does not. We will compare the relative strengths of the two.

The nanomagnets are produced by electron beam evaporation of Co through lithographically defined windows on a resist. If, instead, they were a thin film epitaxially grown on the substrate, then we could

have assumed that the film is pseudomorphic and in that case, the strain in the nanomagnet due to differential thermal expansion would be approximately

$$\varepsilon = \left(\alpha_{\text{PMN-PT}} - \alpha_{\text{Co}}\right)\Delta T$$

where α-s are the thermal expansion coefficients and ΔT is the temperature rise. However, the nanomagnets used here are amorphous or polycrystalline and not a pseudomorphic layer. The actual strain is therefore much less in magnitude than what the above equation predicts. Let us assume therefore that

$$\varepsilon_{\text{actual}} = \xi\left(\alpha_{\text{PMN-PT}} - \alpha_{\text{Co}}\right)\Delta T \qquad \left[\xi \ll 1\right]$$

According to the literature, $\alpha_{\text{Co}} = 13\times10^{-6}$/K and $\alpha_{\text{PMN-PT}} = 9.5\times10^{-6}$/K. We estimated in the paper that the strain generated is about 0.18% based on our MuMax3 modeling. If even half of this was due to thermal effects, then the temperature rise needed for that is $257/\xi$ Kelvin (calculated from the last equation). We do not know what ξ is, except that it must be much smaller than unity. Therefore, in order for the thermally generated strain to be a significant fraction (~50%) of the total strain of 0.18%, the temperature rise due to the laser has to be $\gg 257$ K, which is unlikely at the time scale of laser excitation (femtosecond laser) and the applied pump fluence of 15 mJ/cm^2. Therefore, it stands to reason that the bulk of the strain is generated by the d_{31} and d_{33} coupling of the electric field in the piezoelectric that is modulated by the laser and not by the differential thermal expansion. In other words, the first mechanism is dominant over the second.